JOURNAL OF PROPULSION AND POWER
Vol. 27, No. 1, January–February 2011

Study of Narrowband Radiation Intensity Measurements from Subsonic Exhaust Plumes

David L. Blunck*
U.S. Air Force Research Laboratory, Wright–Patterson Air Force Base, Ohio 45433
and
Jay P. Gore†
Purdue University, West Lafayette, Indiana 47907

DOI: 10.2514/1.47962

Narrowband radiation intensity measurements were obtained of exhaust plumes exiting from a converging nozzle with varying Reynolds numbers ($2.4–6.1 \times 10^5$), Mach numbers (0.4–1.0), and temperatures and species compositions corresponding to low fuel-to-air equivalence ratios (0.17–0.28). The plumes were generated by burning jet A with dry air flowing through a laboratory gas turbine combustor. Radiation intensity measurements were acquired using an infrared camera fitted with a narrowband filter (4.34 ± 0.1 μm). The narrowband radiation intensity leaving a diametric path exhibited a power dependence (2.8) on the equivalence ratio. Smaller changes in the intensity were observed for plumes with near-identical equivalence ratios but varying exit velocities. These smaller changes are attributed to differences in the sensible and kinetic energy and the changes in the mixing rates with ambient air. The magnitude of the radiation intensities emanating from chordlike paths normalized by that emitted from the diametric path (at an identical distance from the nozzle exit) plotted as a function of the distance between these paths show approximately self-similar profiles for some conditions. A departure from the self-similar profiles is observed for conditions where the width of the infrared images contracts significantly. For the test conditions studied, the intensity emanating from the diametric paths first decayed linearly with increasing distance from the nozzle exit and then decayed exponentially with an inflexion point near the end of the plume core.

I. Introduction

NARROWBAND radiation intensity measurements of exhaust plumes exiting from a subsonic axisymmetric nozzle are reported in this work. The effects of varying the equivalence ratio (Φ), Mach number (Ma), and Reynolds number (Re) on the magnitude, decay, and distribution of the radiation intensity are summarized. The results are relevant to the threat of heat seeking shoulder-fired missiles being used against subsonic aircraft [1,2], and applicable to situations where radiative heat transfer from high-temperature jets is important.

Infrared radiation emitted from aircraft plumes is primarily from the hot carbon dioxide and carbon monoxide in the exhaust. The largest emissions are in 4.15–4.45 μm range [3]. Broadening of the spectral lines occurs because of collisional, Doppler line shifting, and Doppler [4] line broadening processes at the elevated temperatures, velocities, and participating media concentrations [5]. Radiation emissions are partially transmitted through the participating media in the atmosphere (e.g. carbon dioxide) [5]. The radiation intensity which reaches the ground after attenuation through the atmosphere is typically for spectra near 4.18 and 4.37 μm [6].

The radiation intensity emitted from the plume core is significantly higher than that from the surrounding mixing layer and region downstream of the core [7]. In the core the temperature and species concentrations at the nozzle exit are maintained [8]. Decher [9] modeled the radiation intensity emitted from the core of plumes exiting from turbofan engines. Radiation emissions were calculated as the size and temperature of the core changed for different nozzle pressure ratios (NPR), exhaust velocities, air bypass ratios, and equivalence ratios. Engine cycles which improved the thermal efficiency typically decreased the infrared radiation emitted from the core. Dix et al. [10] measured the radiation intensity emitted from plumes exiting from notched axisymmetric nozzles. An approximately one-third reduction in radiation intensity was observed when 60° notches were used. This was attributed to a 30% reduction in the core length due to increased entrainment and mixing [10].

Radiation emissions from plumes depend on the temperature and species concentrations within the exhaust flow. Processes which increase entrainment and mixing decrease the temperature and radiating species concentrations more rapidly. Russ and Strykowski [11] reported that jets with initially laminar boundary layers mix and spread more rapidly in comparison to flows with initially turbulent boundary layers due to instabilities which are not dampened in the laminar case. Boundary layers for round jets are initially laminar for Reynolds numbers less than 1×10^5 and are fully turbulent for Reynolds numbers greater than 2.5×10^5 [12]. Russ and Strykowski [11] also found that reducing the density of the flow at the nozzle exit enhances mixing and shortens the potential core. Papamoschou and Roshko [13] noted that increasing the Mach number of a jet decreases the spread of the flow. Zaman [14] reported that increasing the Mach number decreases mixing and increases the length of the potential core because of compressibility effects. Changes in the length of the core with homogenous temperature and species concentrations are similar to the changes in the hydrodynamic potential core.

Radiation measurements of sonic and supersonic exhaust plumes have been emphasized in the literature. Banken et al. [6] measured changes in the spectral radiation intensity emitted from sonic flows with varying NPR and exit temperatures. The spectral intensity typically decreased for increasing NPR and increased for higher total temperatures. Ajdari et al. [15] measured the radiation intensity emitted from sonic and supersonic plumes with varying exhaust temperatures and reducing powers. The radiation intensity emitted from sonic under expanded plumes was initially higher than supersonic plumes, but decayed more rapidly downstream because of increased mixing with the surroundings. Sugiyama et al. [16]

Presented as Paper 2009-1639 at the 47th AIAA Aerospace Sciences Meeting including The New Horizons Forum and Aerospace Exposition, Orlando, FL, 5–8 January 2009; received 2 November 2009; revision received 6 September 2010; accepted for publication 28 September 2010.

*Mechanical Engineer, Combustion Branch, 1950 Fifth Street, Building 490. Member AIAA.
†Vincent P. Reilly Professor, School of Mechanical Engineering, 500 Allison Road. Fellow AIAA.

compared the radiant power (W/sr) of supersonic plumes exiting from rectangular and axisymmetric nozzles. An aspect ratio of three or greater resulted in values less than half of that from the axisymmetric plume when the short side of the rectangular nozzle was viewed.

Varney [17] reported that the magnitude and profile of the static temperature at the nozzle exit are the most significant parameters affecting the radiation emitted from plumes. Other important parameters include the nozzle area, nozzle pressure ratio, equivalence ratio, and turbulence level. Additional literature regarding plume radiation emissions can be found in the review by Mahulikar et al. [18].

The specific objectives of this work are as follows based on the preceding study of the literature:

1) Measure the narrowband radiation intensity emitted from an axisymmetric subsonic plume and characterize the spatial distributions of the time-resolved and ensemble averaged measurements.

2) Determine how variations in temperature and species concentrations resulting from changes in the equivalence ratio affect the radiation intensity magnitude and decay in the axial and radial directions.

3) Assess the importance of kinetic energy, turbulent mixing, and compressibility effects on the radiation intensity.

This work has three primary contributions to plume literature. First, radiation properties of subsonic exhaust plumes are presented. This has application to subsonic aircraft and avoids complexities due to shock structures in the flow. Second, the self-similarity of the radial distribution of the radiation intensity emitted from nonreacting exhaust plumes is reported for the first time. Third, the effect of the conversion of sensible to kinetic energy on radiation emissions is quantified and reported.

II. Experimental Arrangement

A. Plume Generation

Figure 1 illustrates the experimental arrangement used to generate the exhaust plumes. High pressure dry air was supplied to a single cup gas turbine combustor mounted in a pressure vessel. The air mass flow rate ($\dot{m}_a$) was determined by measuring the pressure and temperature upstream of a choked sonic orifice. Air mass flow rates for the tests were between 0.7 and 1.6 kg/s. The air was preheated to a temperature of 420 ± 10 K. Jet A was injected into the combustor through an atomizer and burned. A portion of the air flowed around the primary reaction zone and diluted the combustion products and provided convective cooling of the liner. The fuel mass flow rate ($\dot{m}_f$) was measured using a factory calibrated turbine flow meter. The global equivalence ratio, based on the total fuel and air mass flow rates, is reported for the experiments.

The heated exhaust products flowed from the combustor through a perforated plate and exited through the nozzle. The plate had rings of holes drilled at 10° and was used to pressurize the system and impart swirl to the plume. An axisymmetric nozzle with an exit diameter (D) of 9.1 cm was used. The length of the nozzle was insulated with a ~9 cm layer of insulation to reduce heat loss from the exhaust. The nozzle pressure ratio was typically found from the pressure measured at the nozzle inlet, atmospheric pressure values, and compressible flow relationships. The Mach number was determined from the nozzle pressure ratio.

The temperature of the exhaust (T_n) was measured in the nozzle at an axial location corresponding to a diameter of 11.4 cm. Temperature measurements were acquired using a type K thermocouple and are reported to the nearest 5 K. It was assumed that the temperature measured within the nozzle is the static temperature based on alignment of the sheathed tip, which is roughly parallel to the flow. The temperature at the nozzle exit (T_{exit}) was determined using the temperature measured within the nozzle and isentropic expansion relationships. The temperature of the hot exhaust products

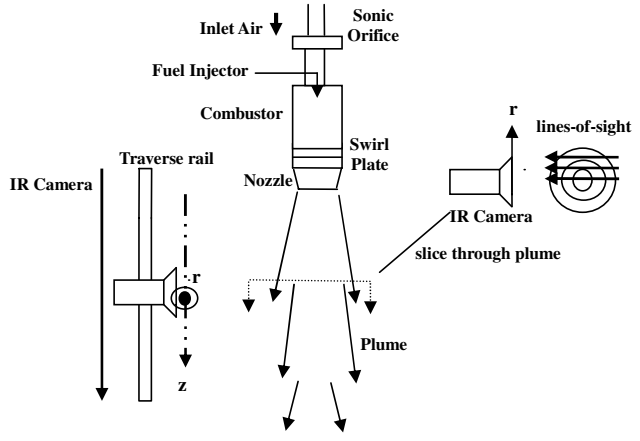

Fig. 1 Experimental arrangement for generating and studying exhaust plumes.

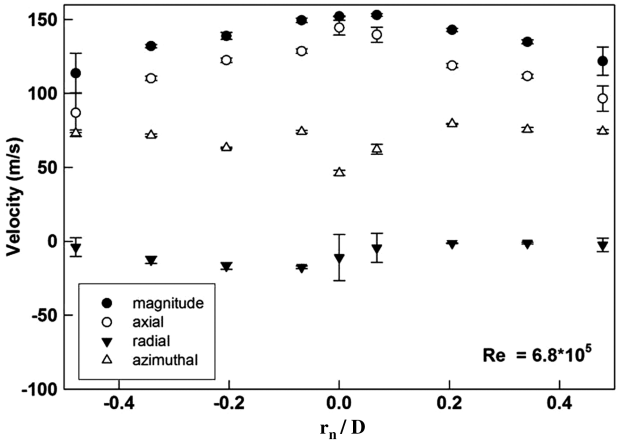

Fig. 2 Velocity distribution at the nozzle exit for flow with representative cold flow conditions.

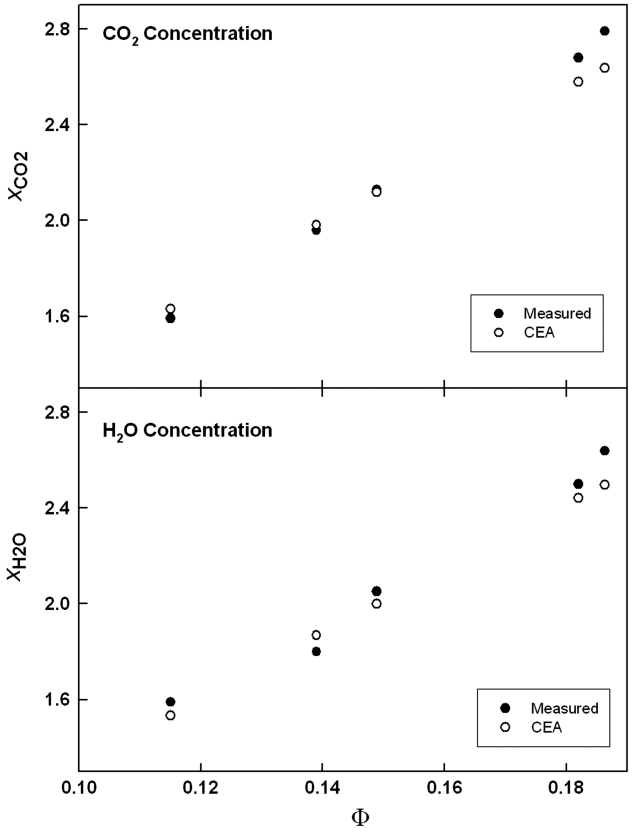

Fig. 3 Measured and calculated H_2O and CO_2 mole fractions for different equivalence ratios.

at the nozzle exit (730–885 K) was within the range reported for plumes by Banken et al. [6] (616–1033 K).

Figure 2 shows measurements of flow velocities in the axial, radial, and azimuthal directions across the nozzle face and plotted with respect to the nozzle radius (r_n) for a representative air flow condition with a Reynolds number equal to 6.8×10^5. The Reynolds numbers of this and all flows in this work are based on the nozzle exit diameter and the properties of air. Velocity measurements were derived from static and dynamic pressure measurements acquired using a multihole pitot probe. Data were acquired without combustion for a total temperature near 300 K and are considered representative of the relative velocity components when combustion is present. The peak total and axial velocities occur in the center of the flow and reduce towards the shear layer. Flow in the radial direction was minimal. Little fluid is entrained into the flow at this (nozzle face) location. The velocity in the azimuthal direction is less than that in the axial direction and is nearly constant across the face of the nozzle. The uncertainty (95% confidence) indicated by the bars on the symbols is based on repeated measurements and suggests confidence in the observed trends.

Mole fractions of exhaust products (X_i) were measured using a Fourier transfer infrared spectroscopy based multigas analyzer and compared with calculations performed using NASA's Chemical Equilibrium with Applications (CEA) solver [19] during a separate experiment. Exhaust samples were obtained downstream of the combustor. Figure 3 shows comparisons between measured and calculated carbon dioxide (CO_2) and water vapor (H_2O) mole fractions for varying equivalence ratios. The measured and predicted concentration values agree within 5%. A 5% error in the species concentrations results in approximately a 2% change in the calculated radiation intensity. The relatively small change in the calculated radiation intensity supports the use of CEA computations for estimating species concentrations of the various test conditions.

It is noted that two primary differences exist between the plumes generated using the experimental arrangement and those expected for aircraft exhaust plumes. First, aircraft plumes are expected to be longer because of the high velocity of the freestream or bypass air. In the present work the surrounding air is stagnant in the vicinity of the experiment. Second, self-absorption of the exhaust plume will become more important as path lengths through the plume increase for larger nozzles. Findings from this laboratory-scale experiment provide insights into the science of exhaust plume radiation and provide a baseline for comparisons with large-scale experiments.

B. Operating Conditions

Table 1 lists the nozzle and exit temperatures, the combustor pressure, air mass flow rate, and velocity for a total of 11 tests. Table 2 presents relevant nondimensional parameters including the equivalence ratio, Mach and Reynolds numbers, and calculated carbon dioxide and water vapor mole fractions. The plume in test 1 was studied to determine (spatially) the regions of peak and minimum intensity, and the radial distribution of the radiation intensity. In tests 2.1–2.5, the effect of the equivalence ratio on the radiation intensity was studied by altering the fuel flow rate for a fixed air flow rate. The equivalence ratio was changed from 0.15–0.27 (80% increase) while the Reynolds and Mach numbers remained within 15% at values of $5.8 - 5.0 \times 10^5$ and 0.7–0.8, respectively. The decrease in the Reynolds number between the tests is because of the temperature dependence of the dynamic viscosity. The increase in the Mach number is because of the inverse dependence of the flow density on the temperature. Tests 3.1–3.5 involved changing the air flow rate to study the effect of changes in the plume velocity on the radiation intensity for similar exit temperatures and species concentrations. For these tests the Mach number changed from 0.4 to 1.0 (130% increase). The Reynolds number varied from 2.4 to 6.1×10^8 (150% increase). It is noted that no shocks were evident in the infrared images for the condition with highest exit velocity indicating that the entire flow field was subsonic. The nozzle pressure ratio was estimated using the measured mass flow rate for test series 3 and using nozzle static pressure measurements for test series 1 and 2. The equivalence ratio was adjusted from 0.17 to 0.19 (10% increase) for test series 3 in order to hold constant the temperature of the exhaust in the nozzle. Holding the temperature at the nozzle exit constant allowed an examination of the influence of kinetic energy.

Table 1 Operating conditions for generating plumes

Test	T_n, K	T_e, K	Combustor pressure, kPa	$\dot{m}_a$, kg/s	V, m/s
1.1	965	885	475	1.4	490
2.1	730	685	415	1.4	370
2.2	785	730	425	1.4	400
2.3	845	785	450	1.4	430
2.4	900	830	460	1.4	450
2.5	950	870	485	1.4	490
3.1	865	770	450	1.6	530
3.2	870	800	365	1.3	450
3.3	865	815	295	1.1	390
3.4	870	835	230	0.9	325
3.5	870	850	165	0.7	250

C. Radiation Measurements

Spectrally integrated radiation intensity (I) measurements were obtained using a FLIR Phoenix infrared camera. The camera measures the line-of-sight spectrally integrated radiation intensity:

$$I_{\Delta\lambda} = \int_{\lambda_1}^{\lambda_2} \alpha_\lambda I_\lambda e^{-\tau_\lambda} \, \mathrm{d}\lambda \tag{1}$$

where α_λ is the total absorption coefficient and accounts for spectral losses in the instrument. The subscript ($\Delta\lambda$) denotes that the measurements are narrowband. Measurements are reported with respect to the camera reference frame, as illustrated in Fig. 1. The spectral intensity can be described by the solution to the radiative transfer equation through a nonscattering medium [20]:

$$I_\lambda = I_\lambda e^{-\tau_\lambda} + \int_0^{\tau_\lambda} I_{b\lambda}(\tau'_\lambda) e^{-(\tau_\lambda - \tau'_\tau)} \tau'_\lambda \, \mathrm{d}\tau'_\lambda \tag{2}$$

where

$$\tau_\lambda = \int_0^s k_\lambda \, \mathrm{d}s \tag{3}$$

and λ_1 and λ_2 is the spectral range allowed by the filter (4.34 ± 0.1 μm). k_λ is the spectral linear absorption coefficient and s is the path length through the plume. The $I_{b\lambda}$ is the spectral blackbody function as defined by Planck's distribution [21]. A narrowband filter was used to decrease influence of background radiation and variations in the spectral response of the detector.

The camera was calibrated following each experiment using an extended area blackbody. The blackbody was placed at the same distance from the camera as the plume centerline. This approach was used to account for atmospheric attenuation of the radiation. Transmission losses through the camera filter and lens as well as the varying spectral response of the camera focal plane array were included in the calibration process. The integration time for the measurements was set to 0.1 or 0.06 ms based on the dynamic range of the detector and the magnitude of the intensity. The sampling frequency was nominally 340 Hz. Mean intensity (I_{mean}) values are based on the average of 300 or more consecutive measurements. A 5% difference in the intensity was noted for values greater than 15% of the peak intensity ($I/I_{\max} > 0.15$) when 1000 measurements were used instead of 300. For smaller intensity values up to a 15% difference was noted. Experiments were performed at night to avoid measuring solar radiation. Values below 2 $\mathrm{W/m^2\text{-}sr}$ are not reported due to the nonlinear behavior of the camera below this limit. This threshold is 5% or less of the peak intensity values measured for the various plumes. Neglecting values below this limit does not affect the conclusions of this work.

The camera was mounted orthogonal to the plume centerline and traversed parallel to the centerline, as shown in Fig. 1. The data were averaged where spatial overlap in the measurements occurred. The spatial resolution of each pixel was typically an area of 0.03 cm^2 at the center of the plume. Every twelfth data point is reported in some figures to avoid clutter.

The change in the width of the infrared images is instructive for characterizing the plumes. This is quantified as half the change in the full width half maximum of the radial distribution of the radiation intensity between axial locations, and is noted as dr/dz. Table 3 reports the change in the width between consecutive nozzle diameters downstream for select test conditions. Many of the spread rates reported in the literature are associated with changes of a point property, such as velocity in a plane [22,23], while the current definition is based on line-of-sight radiation intensities.

D. Uncertainties

The average uncertainty in the intensity and normalized intensity (95% confidence) along the centerline (diametric paths) is 30% and 25%, respectively, until the intensity is 20% of the peak value ($I/I_{max} > 0.2$). For intensity values less than 20% of the peak value ($I/I_{max} < 0.2$), the mean uncertainty is 100 and 120% for the intensity and normalized intensity, respectively. Representative uncertainty bars are reported in the relevant figures. The uncertainty is based on applying a Chi-squared distribution to repeated measurements obtained at one operating condition, following the approach of Moffat [24]. The repeated measurements had an average uncertainty of 20% (95% confidence) for values greater than 20% of the peak intensity and 65% for intensity values less than 20% of the peak value. Measurements were repeated for one condition because the complex nature of the experiment limited repeated measurements at each condition. The uncertainty of the temperature and pressure measurements is 5% based on manufacturer specifications. This results in a 2 and 5% uncertainty in the Reynolds numbers and air mass flow rates, respectively. The Mach number found using the measured nozzle pressure ratio typically agreed within 10% of the value found using the measured air mass flow rate.

III. Results and Discussion of Results

A. General Characteristics

Figure 4 shows four consecutive plume images with an integration time of 0.1 ms. The time elapsed between each consecutive image is 3 ms, yielding the four images within an elapsed time of 12 ms. The highest intensity is represented by the brightest colors. Between axial locations (z) of 0 and 10 cm ($z/D \approx 1$), a high-intensity region ($I > 100$ W/m^2-sr) is observed in the center of the plume. This is surrounded by thin regions of lower intensities ($I \sim 80$, 60 and 40 W/m^2-sr) which result from progressive mixing of the exhaust with the ambient air in the shear layer. The profiles of the higher intensity regions become notably convoluted beyond approximately 10 cm downstream. This corresponds with broadening of the lower intensity region due to the expansion of the shear layer by entrainment and mixing with the surrounding air. By an axial distance of 20 cm ($z/D \approx 2$), the majority of the high-intensity region of the plume fades due to the entrainment and mixing processes driven by the vortical structures, which can be seen near the edges of the images. Beyond an axial location of 20 cm, the plume images narrow until ambient values are approached farther downstream (e.g. $z = 50$ cm, $z/D \approx 5.5$). Small radiating pockets downstream in the flow are observed in some of the snapshots, such as Fig. 4a. This is consistent with the intermittent mixing in the plume, with pockets of exhaust gases existing in the flow as far downstream as 50 cm.

An ensemble average of 300 images with 3 ms between images (averaging time of 0.9 s) is shown in Fig. 4e. The high-intensity region ($I > 100$ W/m^2-sr) begins at the nozzle and tapers to a tip near an axial location of 17 cm. This is primarily radiation emitted from the core, which narrows due to spreading of the shear layer. The low intensity portion of the plume ($I < 100$ W/m^2-sr) starts as a thin annular region surrounding the core and increases in width until it is the broadest between 20 and 25 cm downstream, after which the width decreases due to continued mixing. The high-intensity region ($I > 140$ W/m^2-sr) at the nozzle exit is the radiation emitted from the exhaust and the nozzle wall. Values for axial distances greater than 4 cm are considered in this work to avoid confusing radiation emitted from the nozzle or insulation and that emitted from the plume.

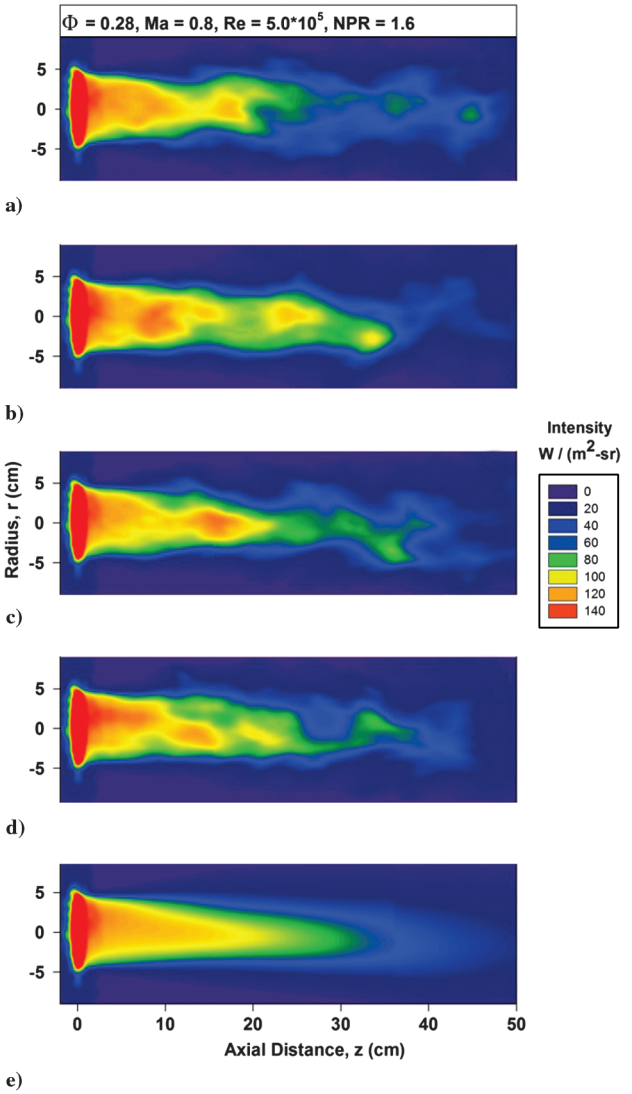

Fig. 4 Instantaneous (A–D) and average (E) intensity measurements.

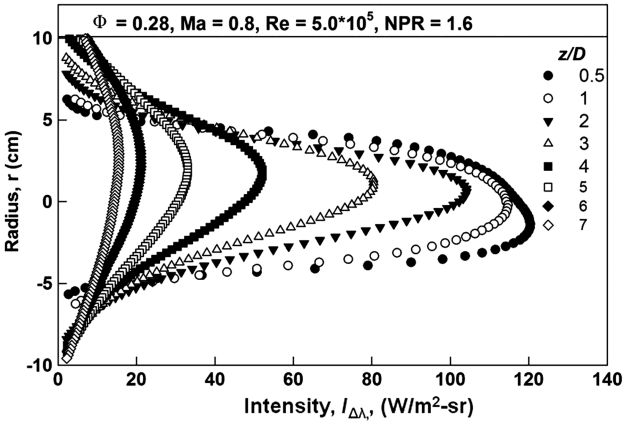

Fig. 5 Plume radiation at seven axial locations.

Narrowband radiation calculations were performed to estimate the contribution of emissions from the heated water vapor and carbon dioxide to the measured intensity. Calculations were performed by solving Eqs. (2) and (3) using RADCAL, a narrowband radiation model [25], and solving Eq. (1) using the calculated spectral intensity. The computations assumed a homogenous path length of 9 cm, carbon dioxide and water vapor mole fractions of 0.039 and 0.037 (respectively), and a temperature of 885 K. These correspond to the conditions for the plume reported in Fig. 4. Note that a homogenous path length of 9 cm is representative of line-of-sight measurements through the plume centerline near the nozzle exit. The calculated radiation intensity neglecting water vapor was within 0.4% of that found including both water vapor and carbon dioxide. This indicates that radiation emissions are primarily from carbon dioxide within the spectral range of the filter.

Figure 5 shows average intensity profiles at axial locations of one-half through seven nozzle diameters downstream for the plume reported in Fig. 4e. The radius is plotted along the y-axis and the intensity along the x-axis. The angle of the plume relative to the horizon is approximately 4°, based on the radial location of the peak intensity. The peak intensity decays with increasing distance downstream due to entrainment and mixing with the ambient air. Between one and two nozzle diameters downstream the width of the thermal image contracts ($dr/dz = -.04$), as defined by the full width at half maximum of the radial distribution of the intensity. The contraction is attributed to shrinking of the core due to mixing with the shear layer. Between two and six diameters downstream the core ends and the annular shear layer expands ($0.02 \leq dr/dz \leq 0.13$). The maximum spread rate (0.13), based on the infrared image, is observed between four and six diameters downstream. Between six and seven and then seven and eight diameters downstream the plume spreads at a reduced rate ($dr/dz = 0.09, 0.05$, respectively). This suggests that the spread of the infrared images is finite, despite the fact that the spread of the exhaust plume eventually becomes independent of the distance downstream [26].

Figure 6 shows the ratio of the average radiation intensity reported in Fig. 4 for varying radial locations (chordlike paths) normalized by the centerline radiation intensity ($I_{\Delta\lambda}/I_{\Delta\lambda,c}$) at eight axial locations. At half a diameter downstream the intensity decays modestly for increasing radii until a normalized radial distance (r/z) of 0.7. The slow decay is due to emissions from the hot exhaust gases in the core. Beyond a normalized radial distance of 0.7, the intensity decreases more rapidly to ambient conditions. Similarly, at one diameter downstream the decay in the normalized intensity is modest until a normalized radial distance of 0.2, beyond which it decays more rapidly. Figure 7 presents an expanded view of the remaining axial locations. At two diameters downstream the core is still evident based on the slower decay in the intensity for increasing radii. By three diameters downstream the effects of the core are no longer observed and subsequently a self-similar profile exists for the normalized intensity, particularly for $I_{\Delta\lambda}/I_{\Delta\lambda,c}$ greater than 50%.

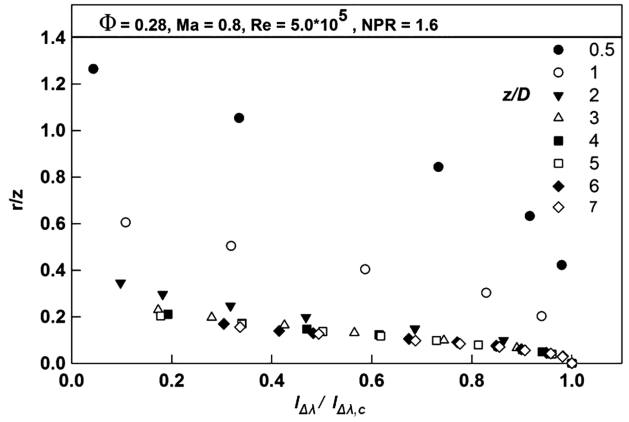

Fig. 6 Radial self-similarity of normalized radiation intensity at eight axial locations.

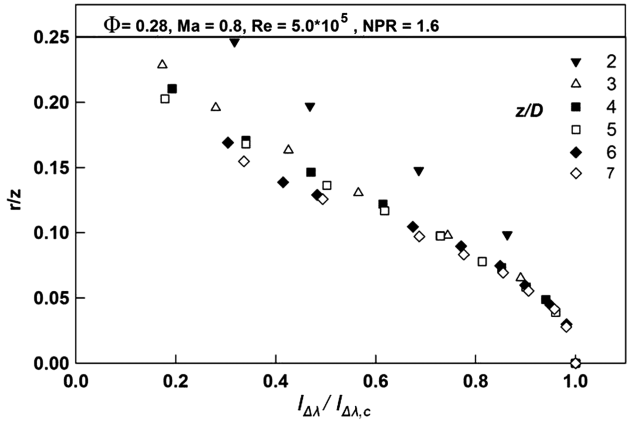

Fig. 7 Radial self-similarity of normalized radiation intensity at six axial locations.

B. Effect of Equivalence Ratio

Figure 8 shows ensemble averages of the radiation intensity emitted from plumes with equivalence ratios of 0.15, 0.21, and 0.27. The distinct lines in the plume with the highest equivalence ratio (A) near an axial location of 30 cm are an artifact of misalignment and do not affect the forthcoming observations regarding the width and length of the images. Qualitatively, the plume with the highest equivalence ratio, had the highest intensity and was longer than the other two plumes. The plume with the lowest equivalence ratio (C) had the lowest intensity and was narrower than the other two plumes. The increase in the magnitude of the intensity and the width of the images as the equivalence ratios was increased results from the higher temperatures and species concentrations.

Figure 9 shows the centerline intensity for tests 2.1–2.5 and is useful for quantifying the changes in the intensity as the equivalence ratio is changed. Near the nozzle exit ($z = 4$ cm) a nearly fourfold increase in the intensity is observed between the plume with an equivalence ratio of 0.15 and 0.27, and a doubling in the intensity emitted from the plumes with equivalence ratios of 0.21 and 0.27. The plume with the smallest equivalence ratio (0.15) had the intensity reduce to less than 2 W/m^2-sr at an axial location of 65 cm. The

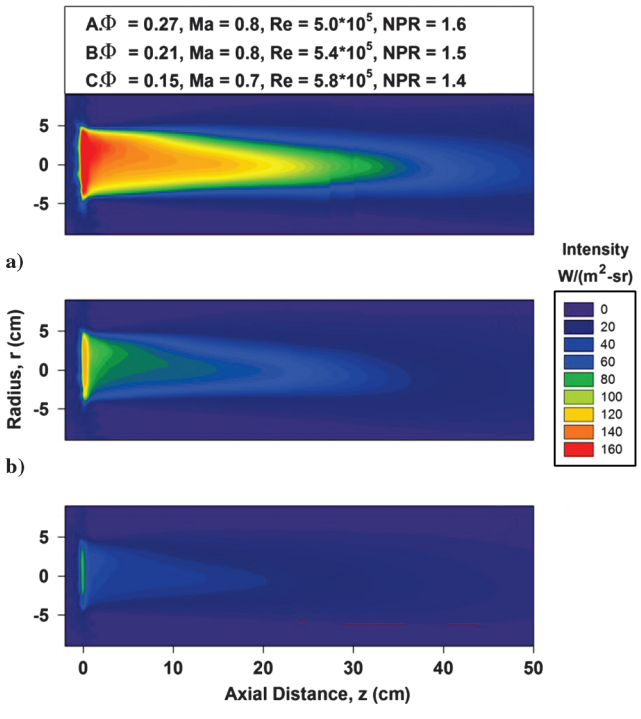

Fig. 8 Average plume intensity for varying equivalence ratios.

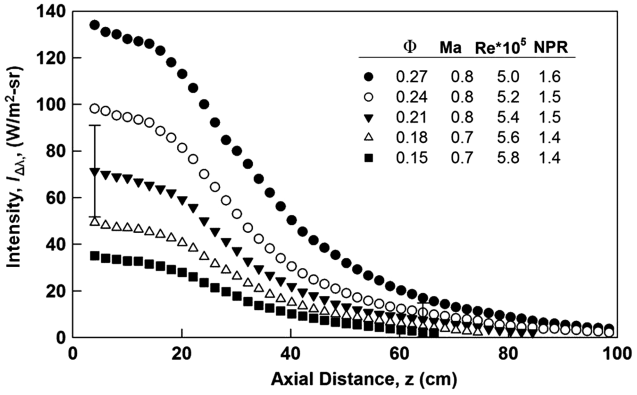

Fig. 9 Intensity along centerline for varying equivalence ratios.

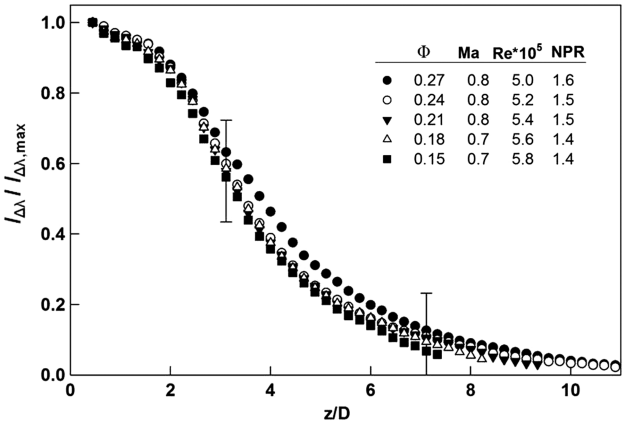

Fig. 10 Intensity decay along centerline for varying equivalence ratios.

plume with the highest equivalence ratio (0.27) had the intensity reduce to less than 2 W/m^2-sr at an axial location of 100 cm. The average power dependence (n) of the intensity on the equivalence ratio

$$\frac{I_a(z)}{I_b(z)} = \left(\frac{\Phi_a}{\Phi_b}\right)^n \tag{4}$$

is 2.8 with a standard deviation of approximately 15%. This is based on the average of ten values of n along the plume axis of each test with respect to the other conditions. The exponential dependence of Eq. (4) is 6 when based on the exit static temperature instead of the equivalence ratio. Banken et al. [6] reported power dependence values between seven and nine for exhaust plumes exiting from converging axisymmetric nozzles.

Narrowband radiation calculations were performed to ascertain the effects of changes in the temperature and radiating species concentrations on the measured radiation intensity as the equivalence ratio was changed. The calculated nozzle exit temperature is 685 and 870 K for equivalence ratios of 0.15 and 0.27, respectively (Table 2). Narrowband radiation intensity calculations [25] using these two temperatures are a factor of three different assuming a homogenous path length of 9 cm with carbon dioxide and water vapor mole fractions fixed at 0.02. A homogenous path length of 9 cm is representative of line-of-sight measurements for a diametric path near the nozzle exit. An increase in the equivalence ratio from 0.15 and 0.27 results in an 80% increase in the carbon dioxide and water vapor mole fractions and a 25% increase in the calculated radiation intensity for a homogenous path length of 9 cm with a uniform (representative) temperature of 800 K.

It is observed in Fig. 9 that the centerline intensity decayed linearly in the plume core region until an approximate axial location of 15 cm ($z/D = 1.6$) for all equivalence ratios. Beyond the plume core region, the intensity decayed exponentially suggesting rapid mixing and decrease of the scalar values. A plausible explanation for the linear decay in the centerline intensity near the nozzle exit is the reduction in the path lengths through the core with increasing

Table 2 Nondimensional parameters for plume operating conditions

Test	Φ	Ma	Re ($\times 10^5$)	X_{CO2}	X_{H2O}
1.1	0.28	0.8	5.0	0.039	0.037
2.1	0.15	0.7	5.8	0.021	0.020
2.2	0.18	0.7	5.6	0.025	0.024
2.3	0.21	0.8	5.4	0.029	0.028
2.4	0.24	0.8	5.2	0.034	0.033
2.5	0.27	0.8	5.0	0.038	0.036
3.1	0.19	1.0	6.1	0.027	0.025
3.2	0.19	0.8	4.9	0.027	0.024
3.3	0.17	0.7	4.1	0.025	0.023
3.4	0.17	0.6	3.3	0.024	0.023
3.5	0.17	0.4	2.4	0.024	0.023

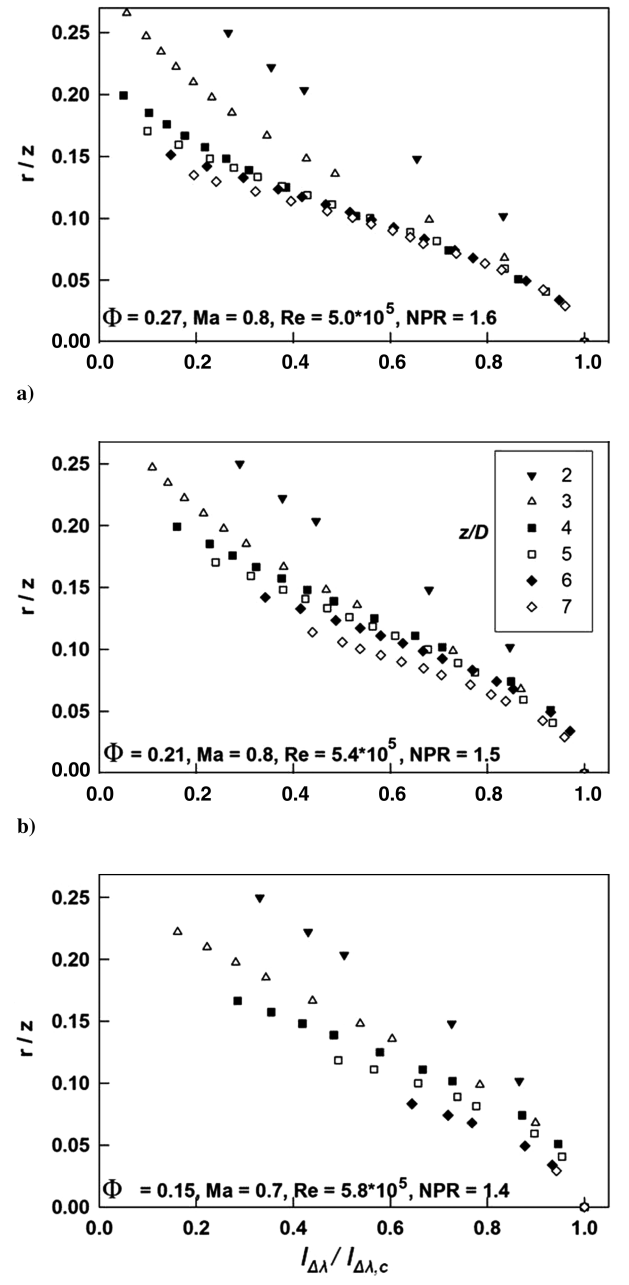

Fig. 11 Normalized radial distribution of plume radiation for varying equivalence ratios.

Table 3 Spread rates for select test conditions

	Test						
	1.1	2.1	2.3	2.5	3.1	3.3	3.5
z/D	Spread Rate (dr/dz)						
0.5–1	——	−0.02	−0.04	−0.04	−0.04	−0.04	−0.04
1–2	−0.04	−0.04	−0.06	−0.06	−0.07	0.00	−0.04
2–3	0.02	0.04	0.03	0.02	0.03	0.05	0.04
3–4	0.10	0.07	0.10	0.02	0.11	0.07	0.13
4–5	0.13	0.04	0.10	0.12	0.13	0.00	−0.01
5–6	0.13	−0.01	0.06	0.10	0.09	−0.05	−0.07
6–7	0.09	——	0.03	0.07	0.03	——	——
7–8	0.05	——	−0.02	0.01	−0.06	——	——

distance from the nozzle exit. This explanation is supported by narrowband radiation calculations [25] that show a nearly linear decay in the radiation intensity with distance ($R^2 = 0.98$ for best fit line) until approximately 14 cm downstream. The narrowband calculations were based on path lengths calculated empirically for a conical core with uniform temperature and radiating species concentrations. A core length of 2.5 diameters was assumed based on temperature measurements of a heated jet of air and reported in the next section. Beyond roughly an axial location of 14 cm (2.5 nozzle diameters) the calculated intensities began to decay exponentially supporting the empirical observations.

Figure 10 shows the normalized decay in the intensity ($I_{\Delta\lambda}/I_{\Delta\lambda,\max}$) along the centerline for varying equivalence ratios. The normalized intensities have little dependence on the equivalence ratio between the nozzle exit and near 3 diameters downstream. For axial distances greater than three diameters the profiles of the plumes with equivalence ratios between 0.15 and 0.24 nearly collapse. The plume with an equivalence ratio of 0.27 decayed more slowly in this region. The similar trends for the majority of the normalized intensity values suggests that changes in the flow caused by variations in the plume density [11] and radiation losses are minimal.

The normalized distribution of the plume radiation intensity for chordlike paths at different radial locations for equivalence ratios of 0.27, 0.21, and 0.15 are illustrated in Fig. 11. The normalized intensity profiles for 0.5 and 1 diameters downstream from the nozzle exit were comparable to those shown in Fig. 6 and are not reported. The core is evident for each of the plumes by the shallow profile at 2 diameters downstream. For the plume with the highest equivalence ratio (0.27), self-similarity is observed for the profiles between ∼4 and ∼7 diameters downstream. For the other two (lower) equivalence ratios, self-similar profiles are less evident. These results are correlated with the width of the images in Fig. 8, as quantified in Table 3. The flow with the highest equivalence ratio contracted between 0.5 and 2 diameters downstream, followed by an expansion until eight diameters downstream. The flow with an equivalence ratio equal to 0.21 had similar trends, although the spread of the plume was more gradual between four and seven diameters downstream. The flow with an equivalence ratio of 0.15 had a contraction in the plume width by six diameters downstream.

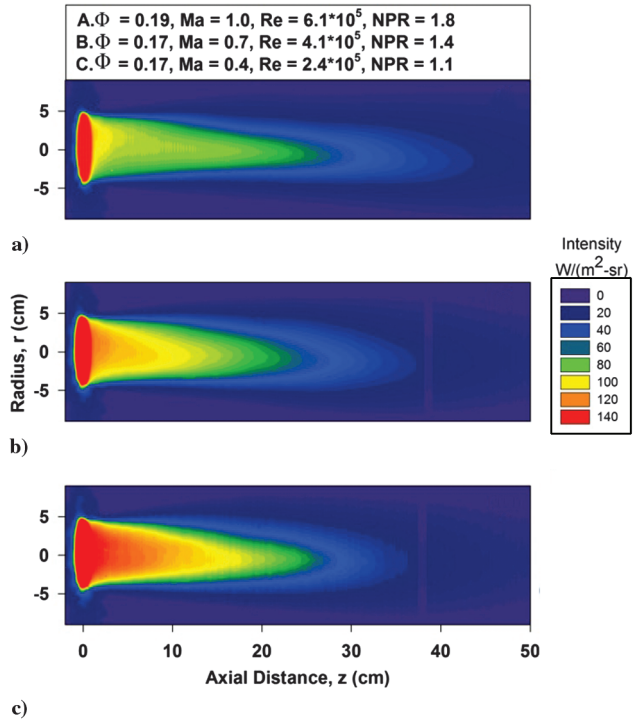

Fig. 12 Average plume intensity for varying Mach and Reynolds numbers.

C. Effects of Reynolds and Mach Numbers

Figure 12 shows the average intensity for plumes with Mach numbers equal to 0.4, 0.7, and 1.0 and Reynolds numbers equal to 2.4, 4.1, and 6.1×10^5 respectively. Shocks were not observed in the flow with the highest Mach number indicating that the flow was subsonic. The light band in Fig. 12 (B) and (C) near an axial location of 37 cm is due to the camera detector behaving nonuniformly for those pixels. The plume with the lowest Mach and Reynolds numbers (*C*) had the highest intensity at the nozzle exit. The plume with the highest Mach and Reynolds numbers (*A*) had the lowest intensity at the nozzle exit. This trend switches and by an axial location of 33 cm the plume with the highest Mach and Reynolds numbers emits the highest intensities. These trends are evident in Fig. 13 which shows the radiation intensity along the centerline for five test conditions with varying exit velocities. An increase of 45% in the centerline intensity is observed between the plumes with the highest and lowest Mach and Reynolds numbers. At an axial location of 30 cm this trend switches and the flow with the highest Mach and Reynolds numbers

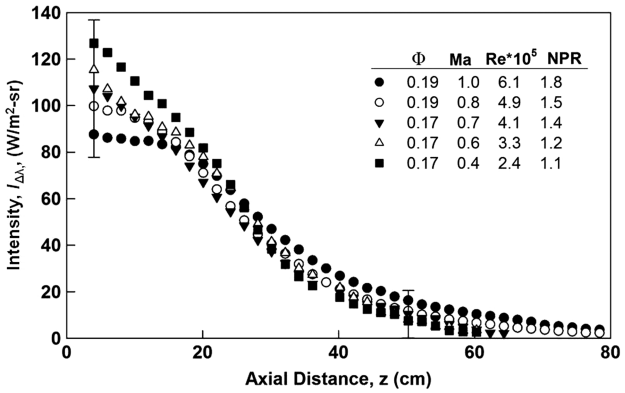

Fig. 13 Intensity along centerline for flows with varying Mach and Reynolds numbers and a fixed temperature in the nozzle.

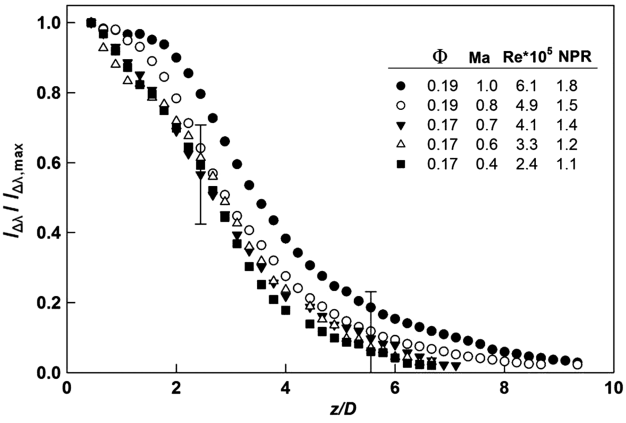

Fig. 14 Normalized centerline intensity for flows with varying Mach and Reynolds numbers and a fixed temperature in the nozzle.

has the highest centerline intensity. Similar to the profiles observed as the equivalence ratio was changed, the decay in the centerline intensity is linear until ∼18 cm ($z/D = \sim 2$) downstream, beyond which the intensity decays in an exponential manner. It is noted that the slope of the linear decay region is greater for the flows with lower Mach and Reynolds and numbers. Figure 14 shows the normalized centerline intensity. It is observed that the larger the exit velocity the more gradual the decay in the centerline intensity downstream.

Changes in the intensity as the Mach and Reynolds numbers are varied are due to changes in the static temperature and mixing rates. The exit temperature increased from 770 to 850 K as the Mach number of the flow was decreased from 1.0 to 0.4. Sensible energy in the flow is converted into kinetic energy. The calculated intensity increases by 55% for this temperature increase assuming a homogenous path length of 9 cm with uniform water vapor and carbon dioxide concentrations (0.025). These calculations are illustrative of the effect of converting sensible energy into kinetic energy can have on the radiation intensity.

Temperature measurements were acquired in heated jets of air to verify changes in the exit values and to provide insights into the temperatures changes downstream in the flow. Figure 15 shows the centerline temperature normalized by the temperature measured in the nozzle for flows with Mach numbers of 0.2–0.6 and Reynolds numbers of $2.7–8.4 \times 10^5$. No combustion was used to avoid damaging the traverse equipment; consequently, results are representative of those for exhaust flows. For a given exit velocity the temperature is uniform until between two and three diameters downstream, indicating that the core ends in this region. The flows with higher exit velocities have smaller normalized temperatures. Downstream of the core region the temperature in the flows with lower velocities decreased more rapidly, in harmony with the trends observed for the centerline intensity. This indicates changes in the mixing and entrainment of the flows. Zaman [12] reported for flows exiting from a converging nozzle that the jet exit boundary layer is fully laminar for Reynolds numbers equal to 1×10^5 and fully turbulent for Reynolds numbers equal to 2.5×10^5. Jets with initially turbulent boundary layers have less entrainment due to disruption of large-scale vortices forming in the flow [11]. The influence of the boundary layer on entrainment in the plumes requires further investigation considering that the Reynolds numbers range from $2.4–6.1 \times 10^5$. A reduction in jet entrainment has been observed as the Mach number of jets is increased [27]. This trend was attributed to changes in the density of the jet [27]. Lau et al. [28] noted that the turbulence levels in flows generally reduced as the Mach number was increased. To summarize, changes in the exit velocity change both the sensible energy and the mixing and entrainment into the flow.

The radial distribution of the radiation intensity is shown in Fig. 16. The profiles for 0.5 and 1 diameter downstream were comparable to those shown in Fig. 5 and are not reported. The core is evident at two diameters downstream for each of the conditions. For the plume with the highest Mach and Reynolds numbers (*A*) self-similar profile are

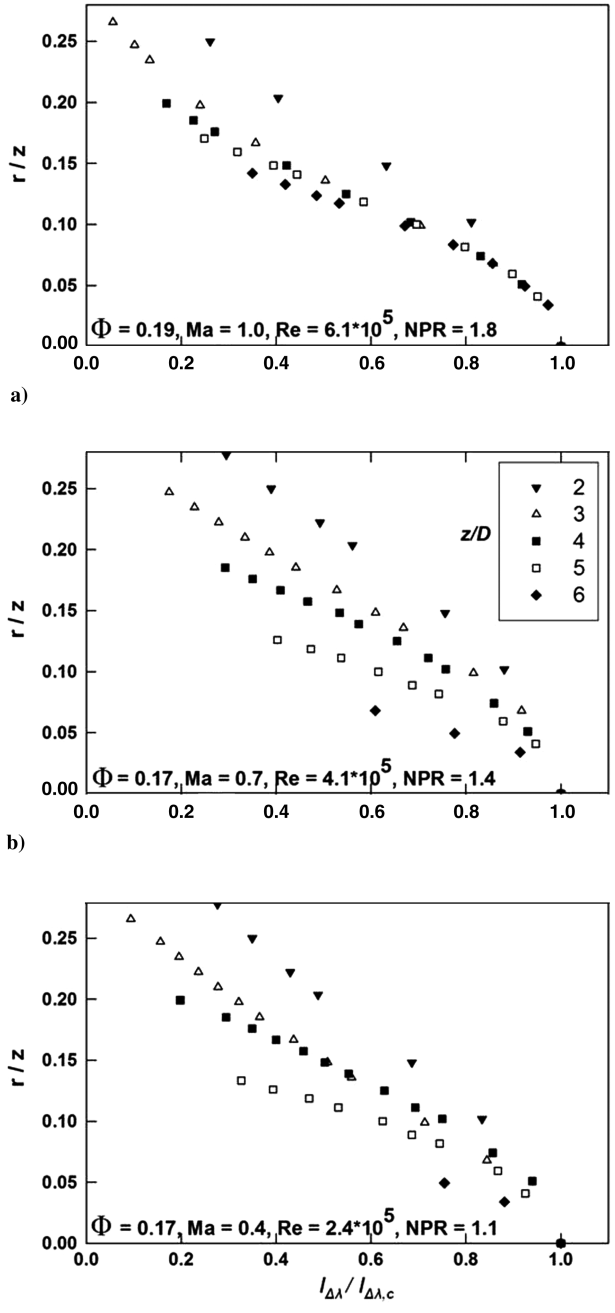

Fig. 16 Normalized radial distribution of plume radiation for varying Mach and Reynolds numbers.

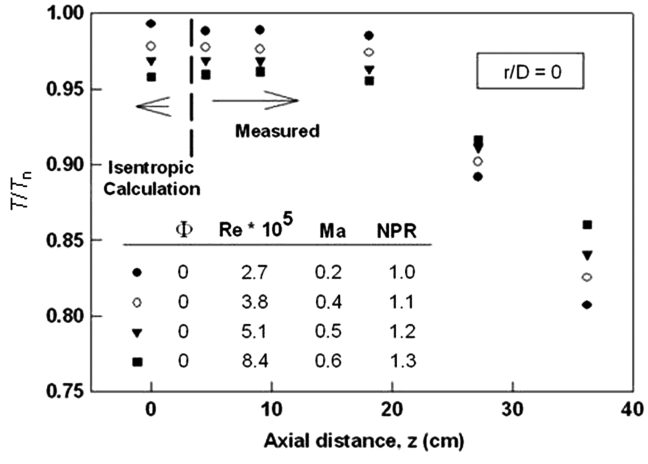

Fig. 15 Axial temperature distribution in heated jets of air.

observed for the normalized intensity for nearly all radial locations. For the plume conditions with lower exit velocities (*B* and *C*) no self-similarity is evident. Again these results are correlated with the spread of the infrared images shown in Table 3. The flow with the highest velocity contracted between 0.5 and 2 diameters downstream, followed by an expansion until between seven and eight diameters downstream. The other plumes contracted between 0.5 and 2 diameters downstream followed by an expansion until between four and five diameters downstream. Comparisons of the self-similar profiles between the plume with the high Mach and Reynolds numbers and the plumes reported in the previous sections showed that the trends in the profiles were similar but did not collapse.

IV. Conclusions

In this work, spectrally integrated narrowband radiation intensity measurements of exhaust plumes were obtained for conditions with varied equivalence ratios and exit velocities. The magnitude, decay,

and distribution of the radiation intensity are reported. The conclusions of this study are as follows:

1) The nozzle exit equivalence ratio (which determines the temperature and CO_2 concentrations) has a strong effect on the radiation intensity. The normalized centerline intensity profile, on the other hand, is less dependent on the nozzle exit equivalence ratio. The axial decay rates of the radiation intensity are dominated by mixing of the plume with the surroundings. As a result, variations in the Mach and Reynolds numbers have a stronger influence on the axial decay rates.

2) A linear followed by an exponential decay in the normalized radiation intensity is observed for all operating conditions. These trends are attributed to changes in the path lengths through the core and entrainment and mixing downstream of the core.

3) Plumes with higher velocities and similar equivalence ratios have lower intensity values in the plume core region, but higher values downstream of the core. These effects are because of changes in the kinetic energy and mixing of the plume with the surroundings.

Acknowledgments

This work was supported by funding from the Naval Surface Warfare Center, Crane Division. The aid of Michael Walls as technical supervisor is greatly appreciated. This work was performed while the corresponding author was a graduate research assistant at Purdue University. The aid of Brent Rankin, Brian Jun, Benjamin Roberts, Aaron Ali-Yap, Mathew Thariyan, and Tony Tang are gratefully acknowledged for help in operating the combustor, acquiring and processing data, and designing the nozzle.

References

[1] Bolkcom, C., Feickert, A., and Elias, B., "Homeland Security: Protecting Airliners from Terrorist Missiles," Congressional Research Service RL31741, Rept. for Congress, 2005.

[2] Maurer, D., Phillips, J., Candon, S., Ricks, A., Guran, E., Cothern, L., Levin, B., Morrison, J., Parker, T., Aiken, M., and Jackson, E., "Nonproliferation Further Improvements Needed in U.S. Efforts to Counter Threats from Man-Portable Air Defense Systems," U.S. General Accounting Office GAO-04-519, Rept. to Congress, 2004.

[3] Rao, G., and Mahulikar, S., "Aircraft Powerplant and Plume Infrared Signature Modelling and Analysis," AIAA Paper 2005-221, 2005.

[4] Hewitt, C., and Black, W., "Effect of Line Doppler Shift on Plume Infrared Signatures," *Journal of Thermophysics and Heat Transfer*, Vol. 9, No. 4, 1995, pp. 636–643. doi:10.2514/3.718

[5] Mahulikar, S., Rao, G., Sane, S., and Marathe, A., "Aircraft Plume Infrared Signature in Nonafterburning Mode," *Journal of Thermophysics and Heat Transfer*, Vol. 19, No. 3, 2005, pp. 413–415. doi:10.2514/1.14686

[6] Banken, G., Cornette, W., and Gleason, K., "Investigation of Infrared Characteristics of Three Generic Nozzle Concepts," AIAA Paper 1980-1160.

[7] Chu, C-W., Der, J., and Wun, W., "Simple Two-Dimensional-Nozzle Plume Model for Infrared Analysis," *Journal of Aircraft*, Vol. 18, No. 12, 1981, pp. 1038–1043. doi:10.2514/3.57597

[8] Heragu, Srinath, Rao, K., and Raghunandan, B., "Prediction of Radiative Transfer from Potential Core of a Hot Jet," *Journal of Thermophysics and Heat Transfer*, Vol. 8, No. 2, 1994, pp. 368–370. doi:10.2514/3.548

[9] Decher, R., "Infrared Emissions from Turbofans with High Aspect Ratio Nozzles," *Journal of Aircraft*, Vol. 18, No. 12, 1981, pp. 1025–1031. doi:10.2514/3.44742

[10] Dix, J., Saddington, A., Knowles, K., and Richardson, M., "Infra-Red Signature Reduction Study on a Small-Scale Jet Engine," *The Aeronautical Journal*, Vol. 109, No. 1092, 2005, pp. 83–88.

[11] Russ, S., and Strykowski, P., "Turbulent Structure and Entrainment in Heated Jets: The Effects of Initial Conditions," *Physics of Fluids*, Vol. 5, No. 12, 1993, pp. 3216–3225. doi:10.1063/1.858678

[12] Zaman, K., "Far-Field Noise of a Subsonic Jet Under Controlled Excitation," *Journal of Fluid Mechanics*, Vol. 152, 1985, pp. 83–111. doi:10.1017/S0022112085000581

[13] Papamoschou, D., and Roshko, A., "The Compressible Turbulent Shear Layer: An Experimental Study," *Journal of Fluid Mechanics*, Vol. 197, 1988, pp. 453–477. doi:10.1017/S0022112088003325

[14] Zaman, K., "Asymptotic Spreading Rate of Initially Compressible Jets-Experiment and Analysis," *Physics of Fluids*, Vol. 10, No. 10, 1998, pp. 2652–2660. doi:10.1063/1.869778

[15] Adjari, E., Gutmark, E., Parr, T., Wilson, K., and Schadow, K., "Thermal Imaging of Afterburning Plumes," *Journal of Propulsion and Power*, Vol. 7, No. 6, 1991, pp. 873–878. doi:10.2514/3.23404

[16] Sugiyama, Y., Adachi, K., and Tokaji, I., "Aspect-Ratio Effects on Infrared Radiation Intensity of 2-D Nozzle Exhaust Plume," *Tenth International Symposium on Air Breathing Engines*, 1991, pp. 1111–1115.

[17] Varney, G., "Infrared Signature Measurement Techniques and Simulations Methods for Aircraft Survivability," AIAA Paper 1979-1186, 1979.

[18] Mahulikar, S., Sonawane, H., and Rao, A., "Infrared Signature Studies of Aerospace Vehicles," *Progress in Aerospace Sciences*, Vol. 43, Nos. 7–8, 2007, pp. 218–245. doi:10.1016/j.paerosci.2007.06.002

[19] CEA2, Chemical Equilibrium with Applications, Chemical Equilibrium Solver, NASA, Cleveland, OH, 2004.

[20] Modest, M., *Radiative Heat Transfer*, 2nd ed., Academic Press, New York, 2003, p. 271.

[21] Siegel, R., and Howell, J., *Thermal Radiation Heat Transfer*, 3rd ed., Hemisphere, Washington, D.C., 1992, pp. 22–27.

[22] Hussein, H., Capp, S., and George, W., "Velocity Measurements in a High-Reynolds-Number, Momentum-Conserving, Axisymmetric, Turbulent Jet," *Journal of Fluid Mechanics*, Vol. 258, 1994, pp. 31–75. doi:10.1017/S002211209400323X

[23] Panchapakesan, N., and Lumley, J., "Turbulence Measurements in Axisymmetric Jets of Air and Helium. Part 1. Air Jet," *Journal of Fluid Mechanics*, Vol. 246, 1993, pp. 197-223. doi:10.1017/S0022112093000096

[24] Moffat, R., "Describing the Uncertainties in Experimental Results," *Experimental Thermal and Fluid Science*, Vol. 1, No. 1, 1988, pp. 3–17. doi:10.1016/0894-1777(88)90043-X

[25] Grosshandler, W., National Institute of Science and Technology TN1402, 1993.

[26] Pope, S., *Turbulent Flows*, Cambridge Univ. Press, Cambridge, England, U.K., 2005, p. 100.

[27] Zaman, K., "Asymptotic Spreading Rate of Initially Compressible Jets: Experiment and Analysis," *Physics of Fluids*, Vol. 10, 1998, pp. 2652–2660. doi:10.1063/1.869778

[28] Lau, J., Morris, P., and Fisher, M., "Measurements in Subsonic and Supersonic Free Jets Using a Laser Velocimeter," *Journal of Fluid Mechanics*, Vol. 93, No. 1, 1979, pp. 1–27. doi:10.1017/S0022112079001750

L. Maurice
Associate Editor